Biomaterials Science

ROYAL SOCIETY OF CHEMISTRY

PAPER

View Article Online
View Journal | View Issue

Cite this: *Biomater. Sci.*, 2024, **12**, 2614

A mitochondria-targeting heptamethine cyanine-chlorambucil formulated polymeric nanoparticle to potentiate native tumor chemotherapeutic efficacy†

Jing Liu,‡[a] Jie Zhang,‡[b] Yongteng Zhang,[d,e] Wei Wei,[b] Meixiao Zhan,[b] Zhiren Zhang,*[b] Bing Liu,*[b] Xianglong Hu *[d,e] and Weiling He*[c]

Received 1st January 2024,
Accepted 6th March 2024

DOI: 10.1039/d4bm00003j

rsc.li/biomaterials-science

Chlorambucil (Cbl) is a DNA alkylating drug in the nitrogen mustard family, but the clinical applications of nitrogen mustard antitumor drugs are frequently limited by their poor aqueous solubility, poor cellular uptake, lack of targeting, and severe side effects. Additionally, mitochondria are the energy factories for cells, and tumor cells are more susceptible to mitochondrial dysfunction than some healthy cells, thus making mitochondria an important target for tumor therapy. As a proof-of-concept, direct delivery of Cbl to tumor cells' mitochondria will probably bring about new opportunities for the nitrogen mustard family. Furthermore, IR775 chloride is a small-molecule lipophilic cationic heptamethine cyanine dye with potential advantages of mitochondria targeting, near-infrared (NIR) fluorescence imaging, and preferential internalization towards tumor cells. Here, an amphiphilic drug conjugate was facilely prepared by covalently coupling chlorambucil with IR775 chloride and further self-assembly to form a carrier-free self-delivery theranostic system, in which the two components are both functional units aimed at theranostic improvement. The theranostic IR775-Cbl potentiated typical "1 + 1 > 2" tumor inhibition through specific accumulation in mitochondria, which triggered a remarkable decrease in mitochondrial membrane potential and ATP generation. *In vivo* biodistribution and kinetic monitoring were achieved by real-time NIR fluorescence imaging to observe its transport inside a living body. Current facile mitochondria-targeting modification with clinically applied drugs was promising for endowing traditional drugs with targeting, imaging, and improved potency in disease theranostics.

Introduction

Tumors remain the most serious disease that threatens human health. The fight against tumors is a major challenge in modern science and biomedicine.[1] Current strategies for tumor treatments mainly consist of surgical resectioning, radiotherapy, and chemotherapy. Although various emerging modalities have been extensively studied, chemotherapy remains the mainstay of clinical tumor treatment.[2] However, conventional chemotherapeutic drugs inevitably face some intractable problems,[3] such as nonspecific biodistribution, lack of selectivity, severe side effects, limited aqueous solubility, low bioavailability, frequent development of multidrug resistance (MDR), and *in vivo* rapid metabolism.[4] In addition, conventional chemotherapy lacks a concurrent diagnostic modality. The development of nanomedicine has brought hope to relieving or even resolving these challenging issues.[5–7] Various nanomedicines have been prepared from organic small molecules,[8,9] polymers,[10–12] and inorganic materials.[13] Their formulated nanostructures mainly exist as liposomes,[14,15] vesicles,[16] micelles,[17] nanosheets[18,19] or nanofibers,[20] which are frequently combined with therapeutic agents and diagnostic probes for kinetic tracing and prognosis monitoring.[21–23]

[a]*College of Biophotonics, South China Normal University, Guangzhou 510631, China*
[b]*Guangdong Provincial Key Laboratory of Tumor Interventional Diagnosis and Treatment, Zhuhai People's Hospital (Zhuhai Hospital Affiliated with Jinan University), Zhuhai, 519000 Guangdong, China. E-mail: zhangzhiren2006@163.com*
[c]*Department of Gastrointestinal Surgery, Xiang'an Hospital of Xiamen University, School of Medicine, Xiamen University, Xiamen, Fujian, 361000, China. E-mail: hewling@mail.sysu.edu.cn*
[d]*Key Laboratory of Precision and Intelligent Chemistry, and CAS Key Laboratory of Soft Matter Chemistry, Department of Polymer Science and Engineering, School of Chemistry and Materials Science, and School of Biomedical Engineering, Division of Life Sciences and Medicine, University of Science and Technology of China, Hefei 230026 Anhui, China. E-mail: huxlong@ustc.edu.cn*
[e]*Suzhou Institute for Advanced Research, University of Science and Technology of China, 215123 Suzhou, China*

†Electronic supplementary information (ESI) available. See DOI: https://doi.org/10.1039/d4bm00003j

‡These authors contributed equally to this work.

However, there are still many uncertainties that constantly hinder the clinical application and achievements of nanomedical technologies,[24,25] such as low drug accumulation, potential toxicity issues associated with overdosing of nanocarrier or ingredients, and limited improvement in therapeutic efficacy, meaning their clinical transformation has a long way to go.[26,27] In this situation, some diagnostic and therapeutic systems formed by the typical covalent binding or physical loading of small-molecular drugs and diagnostic probes are no exception in that diverse nanocarriers are frequently needed to complete the drug delivery process in many cases.[28,29] Based on the abovementioned information, extra-smart carrier-free drug conjugates have attracted increasing attention due to their promising self-assembly characteristics without the aid of nanocarriers,[30–33] and the potential immunotoxicity caused by nanocarriers is expected to be avoided to some extent.[34,35] Some old chemotherapeutic drugs are called alkylating agents, because they can kill tumor cells by alkylating DNA to inhibit tumor growth.[36] Chlorambucil (Cbl) is a type of traditional DNA alkylating agent. Although Cbl is a clinically approved drug, its low water solubility, poor cellular uptake, poor targeting, and susceptibility to rapid degradation in an aqueous environment lead to a short half-life *in vivo*, often requiring a higher dosage to achieve the desired therapeutic effect; however, increasing the dosage can induce a high risk of serious side effects due to off-target alkylation, which definitely limits its extensive clinical application.[37] Therefore, it is necessary to further optimize Cbl, improve its solubility and stability, and increase its accumulation at the site of action to achieve improved efficacy and reduced side effects.[38,39]

In addition, mitochondria have become an important target for tumor therapy due to their unique functions. Currently, many chemotherapeutic agents are used in combination with the mitochondrial therapy to be further optimized. A mitochondrion is an essential organelle that is indispensable for the production of intracellular energy.[40] Notably, the number and metabolic activity of mitochondria in tumor cells have been proven to be higher than those of normal cells, and their rapid proliferation is dependent on sufficient energy and biosynthetic products being produced by mitochondria.[41] In addition, the intrinsic mitochondrial membrane potential of tumor cells is higher than that of normal cells,[40] which makes the mitochondria of target cells targetable by lipophilic cations.[42,43] Heptamethine cyanine dyes have lipophilic cationic moieties, making them potentially able to target mitochondria.[44,45] Some of them can selectively accumulate in tumor cells due to the overexpression of organic anion-transporting polypeptides.[46,47] This unique feature has inspired their employment for tumor imaging and targeted therapy.[48,49] Notably, IR775 chloride, a heptamethine cyanine dye, which has not yet been widely explored for tumor theranostics, also shows good biodegradability, potential mitochondrial targeting, and multiple imaging capabilities.[47,50,51]

In this work, a mitochondria-targeting prodrug conjugate was facilely developed *via* covalent modification of a traditional alkylating chemotherapeutic drug (Cbl) with IR775 chloride, affording the resultant IR775-Cbl with enhanced water solubility and cellular uptake compared to Cbl, with tumor cell mitochondria targeting capability and significantly higher molar potency for tumor treatment, which not only increases the accumulation of therapeutic agents at the site of action but also reduces potential toxicities associated with potential off-target alkylation (Scheme 1). The aqueous self-assembly of IR775-Cbl could readily formulate into narrowly dispersed nanoparticles in the absence of additional excipients. Upon efficient cellular uptake and mitochondrial targeting towards tumor cells, remarkable mitochondrial dysfunction and rapid cell death were achieved towards tumor cells *in vitro*. The presence of the IR775 moiety afforded the resulting drug conjugate with near-infrared (NIR) fluorescence for *in vivo* tumor imaging. The mitochondria-targeting heptamethine cyanine-chlorambucil formulated polymeric nanoparticle was evaluated to exhibit typical "1 + 1 > 2" tumor inhibition efficacy *in vivo* compared with that of Cbl and IR775.

Results and discussion

Preparation and characterization of the IR775-Cbl conjugate

As depicted in Scheme 1 and Scheme S1,† IR775-Cbl was obtained by a facile two-step procedure. First, IR775-OH was obtained from the replacement of meso-Cl in IR775 by the thiol group of 3-mercapto-1-propanol in *N*,*N*-dimethylformamide (DMF), affording the intermediate with a yield of ~63%.[44] As indicated in the ^{1}H HNR spectrum of IR775-OH (Fig. S1†), the meso-Cl of IR775 was replaced readily by the thiol group, suggesting its successful preparation. The final drug conjugate IR775-Cbl was obtained by the reaction of IR775-OH and Cbl under the catalysis of 1-(3-dimethylaminopropyl)-3-ethylcarbodiimide hydrochloride (EDC) and 4-dimethylaminopyridine (DMAP)[52] and was characterized by its ESI-HRMS, ^{1}H NMR and ^{13}C NMR spectra (Fig. S2–S4†). The photophysical features of IR775-Cbl were then examined accordingly. The UV-vis absorption spectra of IR775-Cbl, IR775, and Cbl dissolved in DMSO showed that IR775 had a characteristic absorption at ~795 nm in the NIR region, Cbl had a peak at ~265 nm, and IR775-Cbl showed slight red-shifting of the characteristic absorption of IR775 and Cbl, which further confirmed the successful conjugation of IR775 and Cbl into the resultant IR775-Cbl (Fig. 1A).

Benefiting from the existence of hydrophobic and hydrophilic segments in IR775-Cbl, its aqueous self-assembly was performed *via* typical solvent displacement in the absence of any additives. The absorption spectrum of its aqueous dispersion was further recorded for deliberate observation (Fig. S5†), and the absorption at 600–900 nm was obviously broadened with wide double peaks. The two peaks are the characteristic absorption peaks of typical H-aggregates, which presumably resulted from molecular intermolecular and intramolecular interaction of IR775-Cbl in self-assembled aggregates.[53,54] Then, the fluorescence emission spectra of IR775-Cbl were recorded in DMSO and water, corresponding to

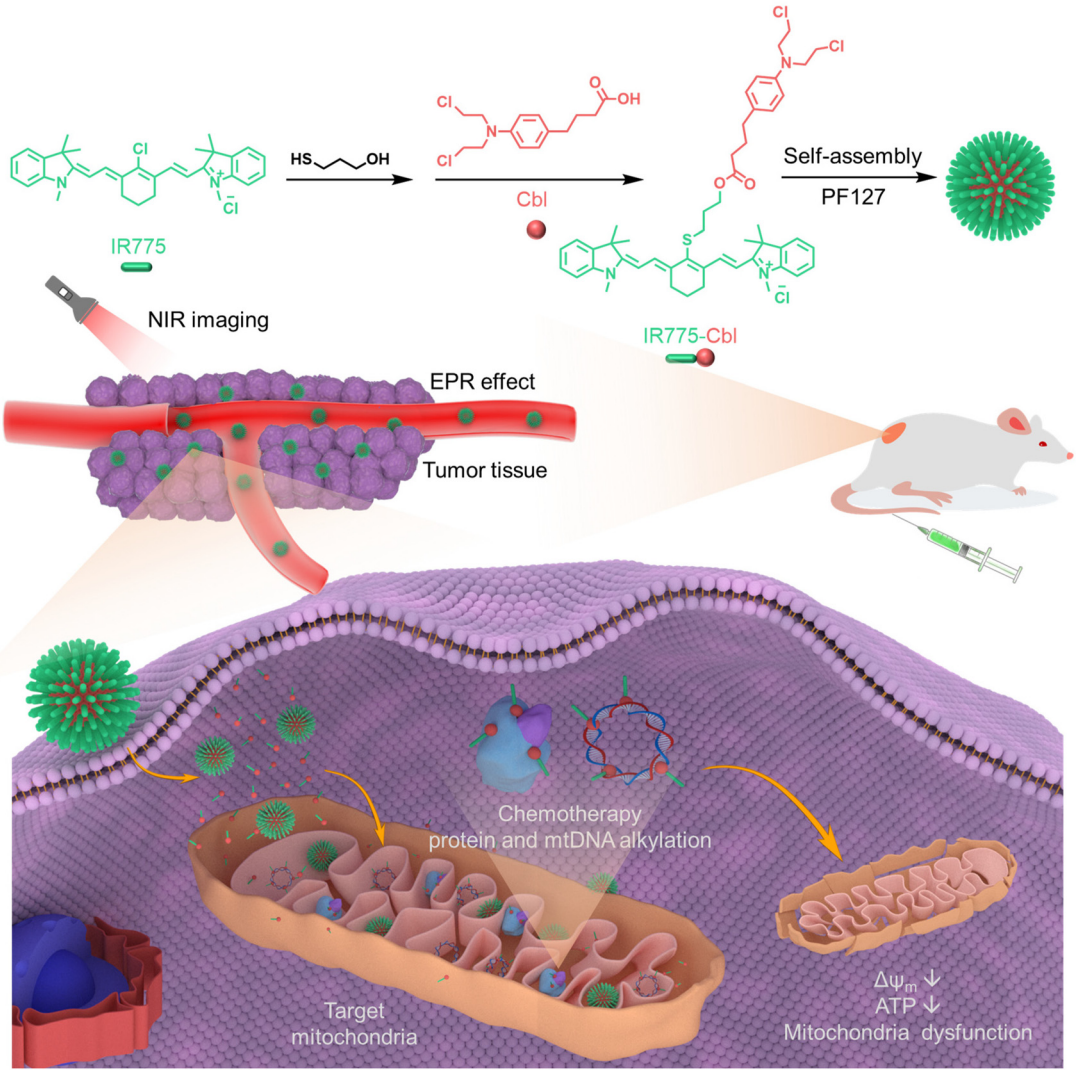

Scheme 1 Schematic illustration of the synthesis of heptamethine cyanine-chlorambucil conjugate (IR775-Cbl) as well as its formulation with Pluronic F-127 (PF127) into polymeric nanoparticles for tumor theranostics. IR775-Cbl can induce specific mitochondrial dysfunction and trigger rapid cell death by bringing alkylating agents into the mitochondria and undergoing probable alkylation, and its efficacy is much higher than that of Cbl or IR775, achieving a "1 + 1 > 2" therapeutic effect.

the free molecular state and aggregation state, respectively (Fig. 1B). The emission intensity of IR775-Cbl in aqueous solution was much weaker than that in DMSO at the same content, which probably resulted from the aggregation-caused quenching (ACQ) effect in the aggregates.[55]

In addition, the fluorescence intensity of IR775 in water was decreased compared to that in DMSO, but not as much as that of IR775-Cbl. This may be due to IR775-Cbl being able to actively self-assemble in water, resulting in a stronger ACQ effect (Fig. S6†). After that, dynamic light scattering (DLS) and transmission electron microscopy (TEM) were utilized to characterize the size and morphology of IR775-Cbl aggregates in water. The zeta potential was recorded to be about +35 mV due to the lipophilic cationic moiety within the IR775 part. Many spherical nanoparticles with a relatively narrow distribution were found to be ~70 nm in the TEM image, and the average hydrodynamic diameter was determined to be ~100 nm, which was larger than that found by TEM analysis. The aqueous dispersion was green and uniform, as observed from the sample photograph (Fig. 1C inset). Finally, the stability of IR775-Cbl aggregates was examined after one week of storage at room temperature, and the size variation was not obvious, suggesting favorable stability for the self-assembled drug aggregates (Fig. 1D).

Cellular uptake and mitochondrial targeting of IR775-Cbl

The cellular uptake and intracellular trafficking of IR775-Cbl nanoparticles were detected by CLSM imaging (Fig. 2A). EMT6 cells were pretreated with IR775-Cbl for 1 h to 12 h, and mitochondria were co-labeled with Mitotracker Green. CLSM imaging showed that the red fluorescent pixels of IR775-Cbl co-localized well with the green pixels of the mitochondria.

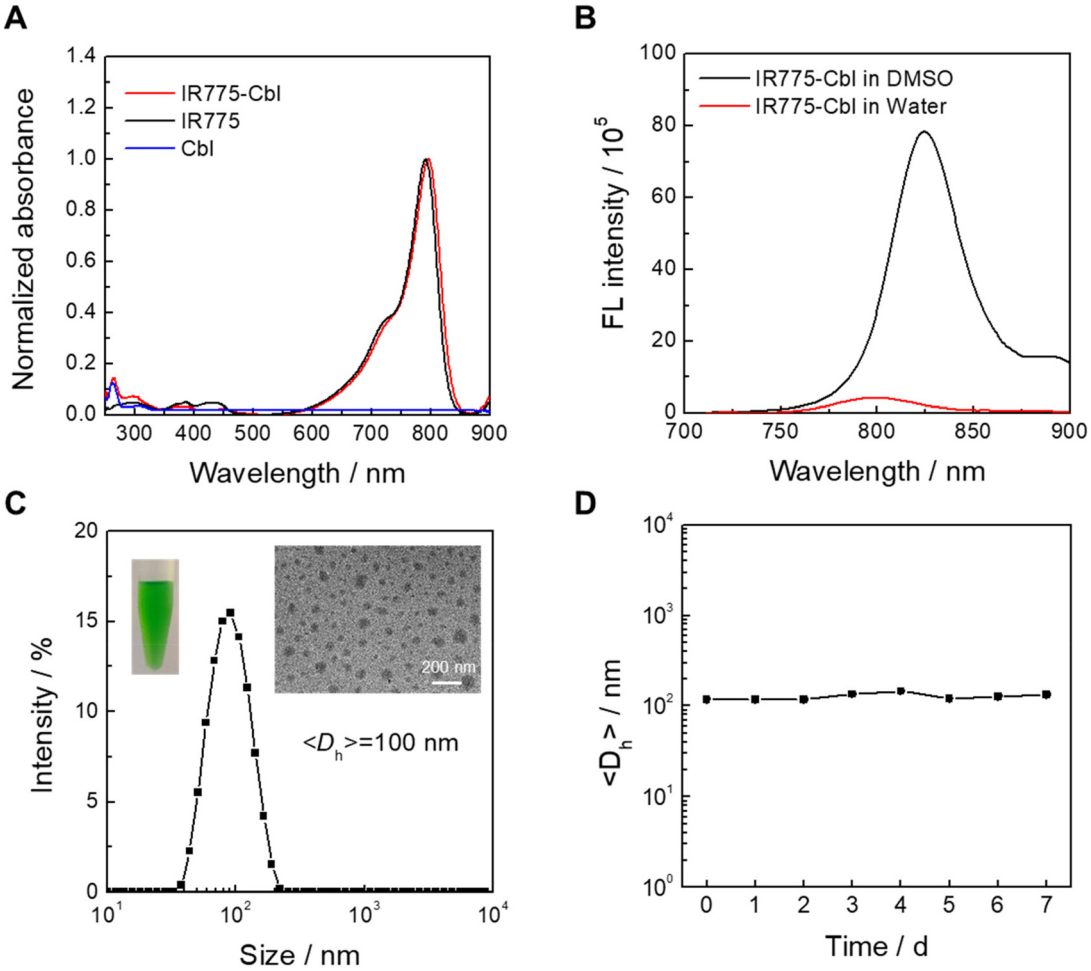

Fig. 1 Chemical characterization of IR775-Cbl and its aqueous self-assembly. (A) Absorbance spectra recorded for IR775-Cbl, IR775 and Cbl in DMSO. (B) Fluorescence spectra obtained for IR775-Cbl in DMSO and its aqueous dispersion. (C) Hydrodynamic diameter distribution recorded for the aqueous dispersion of IR775-Cbl. Insets: its typical TEM image and photograph. (D) Hydrodynamic diameters recorded for the aqueous dispersion of IR775-Cbl at room temperature.

Their corresponding co-localization analysis confirmed remarkable mitochondrial co-localization even after 12 h of incubation, which benefited from the lipophilic cationic moiety of the IR775 segment in IR775-Cbl,[56] and Pearson coefficients were all around 0.6, indicating effective co-localization. Another compound, TPE-Cbl, was successfully synthesized as a control (Fig. S7†). The CLSM images of cells incubated with TPE-Cbl indicated minimal mitochondrial co-localization with the Pearson coefficients determined to be less than 0.1 (Fig. S8†). Herein, the mitochondria targeting ability of IR775-Cbl presumably resulted from the IR775 moiety. Furthermore, flow cytometry analysis was employed to quantitatively analyze the cellular uptake of IR775-Cbl upon diverse incubation durations, suggesting a time-dependent endocytosis process (Fig. 2B and C). In addition, EMT6 cells and normal macrophage Raw 264.7 cells were incubated with the aqueous dispersion of IR775-Cbl. Flow cytometry analysis showed that the rate of IR775-Cbl uptake by tumor cells was much higher than that of normal cells; specifically, the internalization of EMT6 cells was ~2.5-fold compared to that for Raw 264.7 cells upon 12 h of incubation (Fig. S9†). It was speculated that IR775-Cbl could promote active transport into cells *via* organic anion-transporting polypeptides (OATPs) overexpressed on tumor cells,[46] which indicated that IR775-Cbl could be preferentially taken up by tumor cells. EMT6 cells pretreated with the OATPs inhibitor, sulfobromophthalein sodium (BSP), exhibited decreased uptake of IR775-Cbl compared with unpretreated cells, which further supports above-mentioned findings (Fig. S10†).

In situ mitochondrial damage triggered by IR775-Cbl

As examined above, the covalent conjugation of IR775 with Cbl endowed IR775-Cbl with mitochondria targeting potency, which probably improved the therapeutic efficacy.[42,57] In addition, the mitochondrial morphology was observed by CLSM imaging *via* co-staining with Mitotracker Green (Fig. 3F). The mitochondrial morphology in the groups of Cbl, IR775, and the mixture of IR775 and Cbl was close to that of

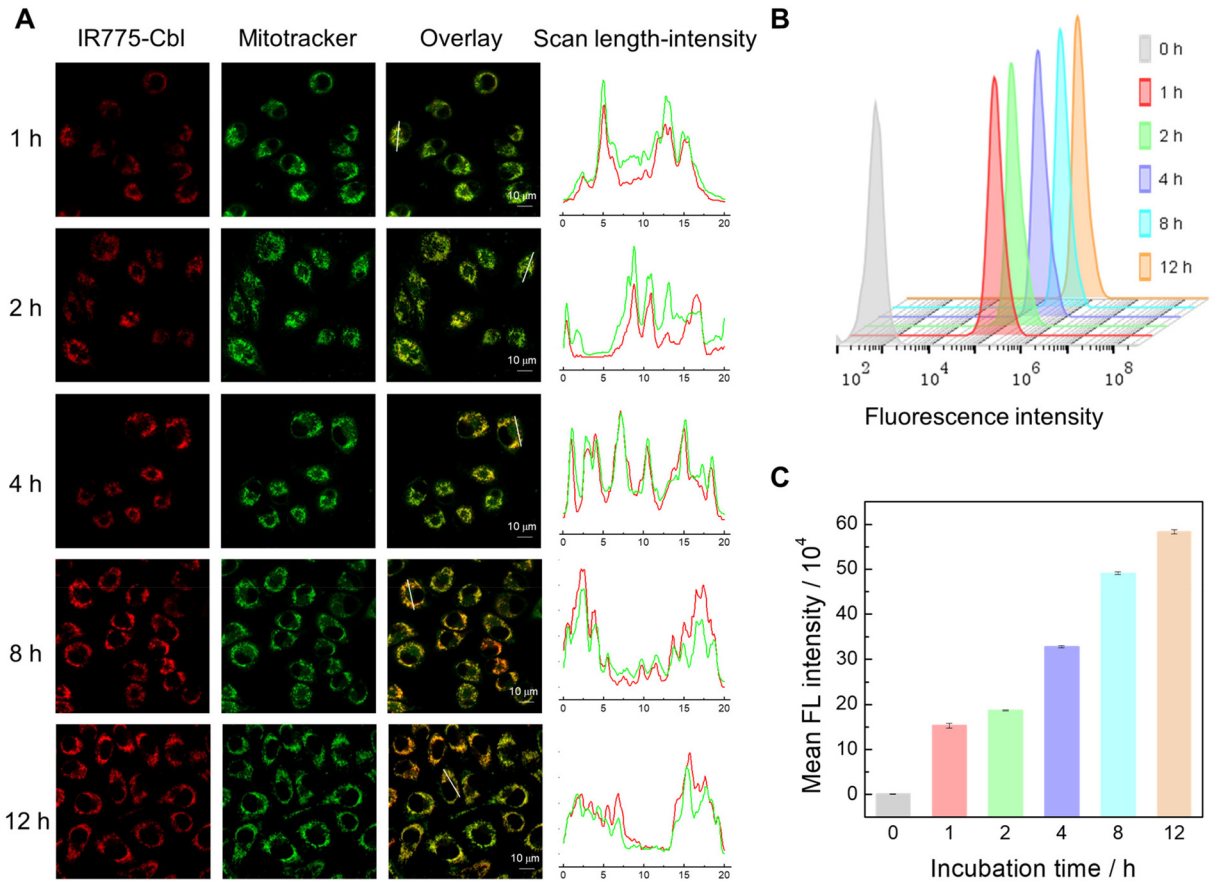

Fig. 2 Cellular uptake and intracellular trafficking of IR775-Cbl. (A) Confocal laser scanning microscopy (CLSM) images of EMT6 cells upon incubation with IR775-Cbl for varying durations at ~1 μM. Mitochondria were co-stained with Mitotracker Green (green channel). (B) Flow cytometry analysis of EMT6 cells upon incubation with IR775-Cbl for different durations at ~5 μM. (C) Statistical analysis of the mean fluorescence intensity in (B).

the untreated control group with a pristine rod structure, whereas the treatment with IR775-Cbl was observed to afford the fragmented and dispersed morphology corresponding to mitochondrial damage.[58] The damage to the mitochondria was further visualized by transmission electron micrograph (TEM) analysis (Fig. 3G). The blank and control groups show normal mitochondria with clear cristae and intact membranes (white arrows), whereas in the electron micrographs of IR775-Cbl-treated cells, the mitochondria were found to be severely damaged, showing vacuoles and membrane degradation (red arrows).

First, CLSM imaging of EMT6 cells after diverse treatments was performed by co-staining with Rhodamine 123 (Rh123) to detect mitochondrial membrane potential that was closely related with mitochondrial functions and integral to various cell death and survival pathways (Fig. 3A).[59] The fluorescence intensity of Rh123 in the IR775-Cbl group decreased dramatically, indicating a significant decrease in mitochondrial membrane potential. The fluorescence signal of the Cbl group was like that of the untreated group; thus, Cbl did not induce obvious mitochondrial damage or dysfunction. This indirectly reflected that Cbl itself found it hard to approach mitochondria. In addition, a subtle decrease in fluorescence was found for the IR775 group as well as the IR775/Cbl mixture group compared with the blank group, which probably resulted from the entry of IR775 into the mitochondria.

Second, another probe, JC-1, a sensitive marker for mitochondrial membrane potential, was further adopted to stain the cells after diverse treatments to examine the states of mitochondrial membrane potential (Fig. 3B). CLSM imaging revealed that the green fluorescence in the IR775-Cbl group was significantly stronger than the red fluorescence, and the red fluorescence corresponding to the J-aggregate almost disappeared.

On the contrary, the untreated control group and the three extra groups all exhibited strong red fluorescence and relatively weak green fluorescence, and a gradual fluorescence transition from red to green indicated a significant loss of mitochondrial membrane potential and probable depolarization of the mitochondria. The result indicated prominent mitochondrial damage of tumor cells upon treatment with IR775-Cbl. Furthermore, the change in the ratio of red to green fluorescence was used as an indicator of the mitochondrial condition,[60] which was quantitively determined by FACS analysis

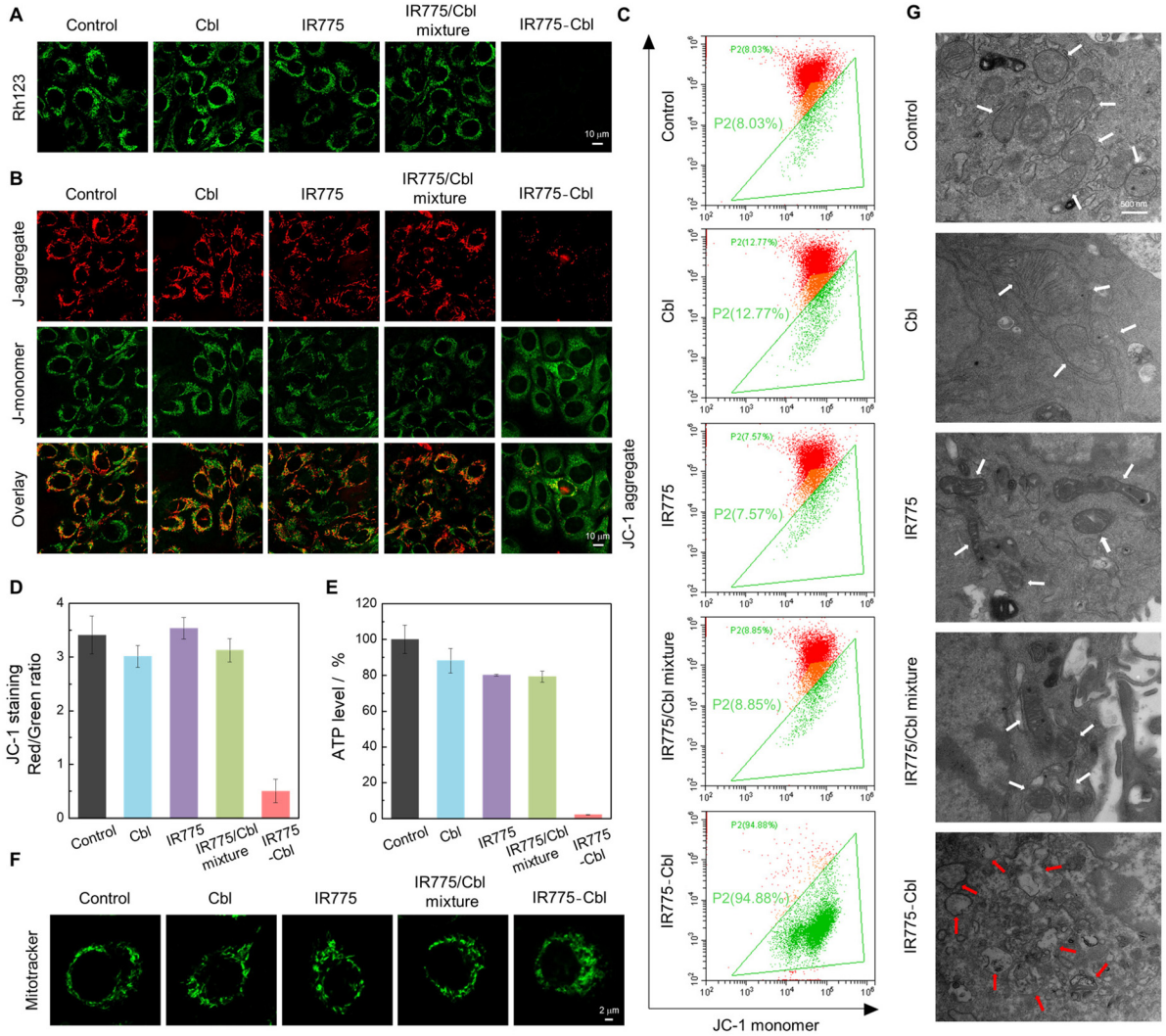

Fig. 3 *In vitro* evaluation of mitochondrial damage initiated by the IR775-Cbl conjugate. (A) CLSM images of Rh123-stained EMT6 cells after different treatments for 6 h at ~2.5 μM. (B) CLSM images of JC-1-stained EMT6 cells upon diverse treatments for 6 h at ~2.5 μM. (C) Flow cytometry analysis of JC-1-stained EMT6 cells after different treatments for 8 h to evaluate the mitochondrial membrane potential at ~2.5 μM. (D) Statistical analysis of fluorescence intensity in (C). (E) Relative ATP levels for EMT6 cells upon diverse treatments for 24 h at ~2.5 μM (mean ± SD, n = 3). (F) CLSM imaging of mitochondrial morphology in EMT6 cells after diverse treatments for 8 h at ~10 μM; the cells were stained with Mitotracker Green. (G) Transmission electron microscopy (TEM) micrographs of EMT6 cells. The control group shows normal mitochondria with clear cristae and intact membranes (white arrows), while the IR775-Cbl group image shows severely damaged mitochondria showing vacuoles and membrane degradation (red arrows).

via JC-1 staining (Fig. 3C and D). The flow cytometry dot plot showed the gating of JC-1 (red)-aggregates and JC-1 (green)-monomer populations. The increasing ratio of red to green fluorescence further verified the impairment of mitochondrial membrane potential upon incubation with IR775-Cbl. These results indicated that treatment with IR775-Cbl could trigger the depolarization of the mitochondrial membrane as well as the resulting dysfunction, which would initiate subsequent apoptosis and necrosis of tumor cells.[60]

To further evaluate the mitochondrial dysfunction, the cellular ATP level was accordingly measured for these groups (Fig. 3E). When EMT6 cells were incubated with different samples for 24 h, the ATP production was analyzed for these groups. The resultant IR775-Cbl group showed the most significant ATP decrease, up to ~98%. These observations definitely demonstrated that IR775-Cbl could induce mitochondrial dysfunction of tumor cells.[61]

In vitro cytotoxicity and cell apoptosis

Mitochondrial dysfunction is associated with mitochondria-associated cell death pathways.[42] Potential cell apoptosis and necrosis induced by IR775-Cbl were analyzed by flow cytometry with Annexin V-FITC/Propidium iodide (PI) double staining (Fig. 4A and B). EMT6 cells were incubated with Cbl, IR775 or IR775/Cbl mixture, and resultant IR775-Cbl nanoparticles, and the untreated group served as a control. The flow cytometry

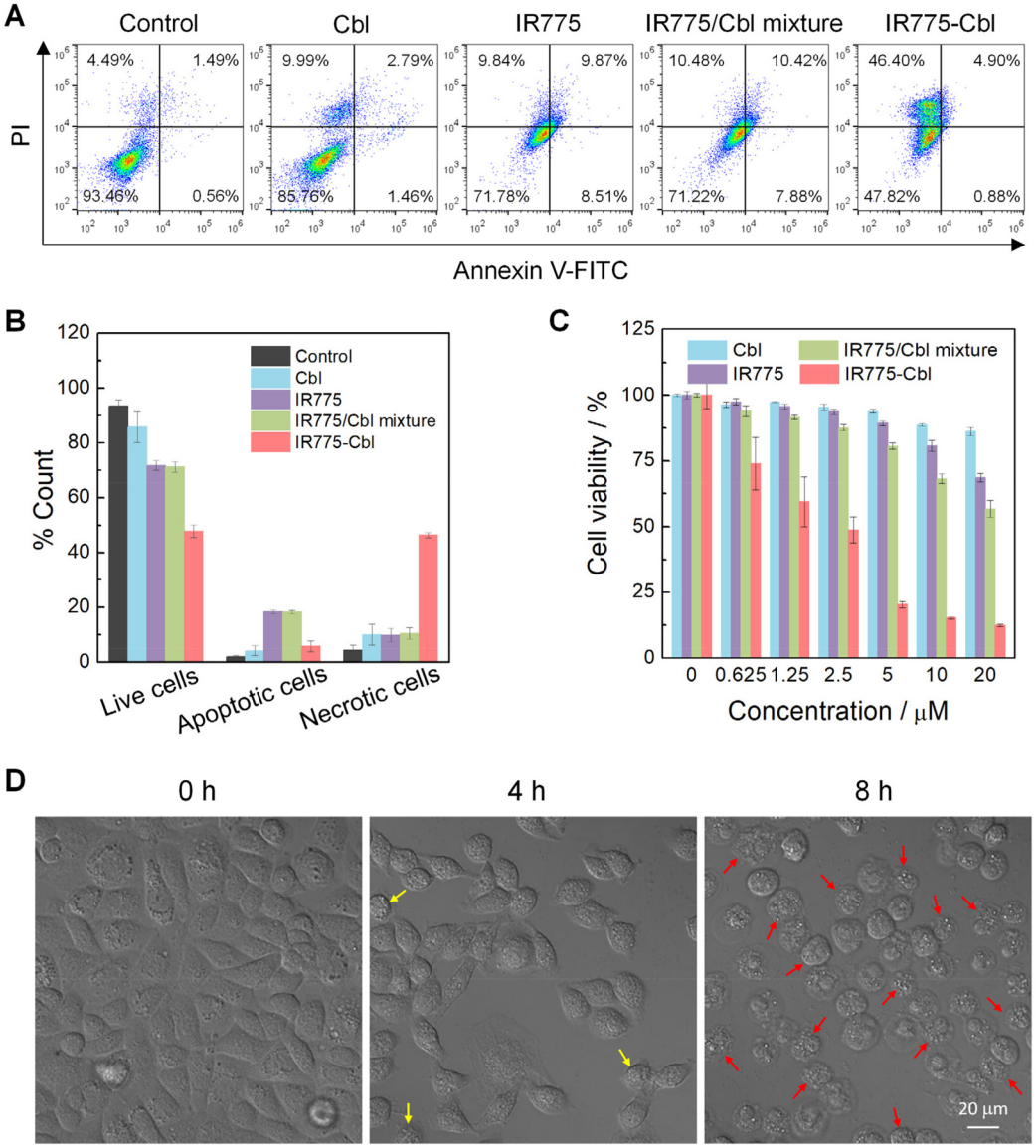

Fig. 4 *In vitro* cytotoxicity evaluation of IR775-Cbl. (A) Cell apoptosis and necrosis analyzed by a flow cytometer with Annexin V-FITC/PI double staining after different treatments at ~10 μM. (B) Statistical analysis of flow cytometry data in (A) (mean ± SD, n = 3). (C) Cell viability determined by an MTT assay for EMT6 cells after different treatments for 48 h. (D) Bright field images of EMT6 cells upon incubation with IR775-Cbl for different durations at ~10 μM. Yellow arrows indicate the typical shrinkage tendency of cells, and red arrows indicate some shrunken, rounded cells under the influence of the drug conjugate.

analysis showed that the percentage of normal cell numbers in the control, Cbl, IR775, IR775/Cbl mixture and IR775-Cbl groups were ~93.46%, ~85.76%, ~71.78%, ~71.22% and ~47.82%, respectively, and the proportions of necrosis induced by Cbl, IR775 and the IR775/Cbl mixture were ~9.99%, ~9.84%, and ~10.48%, while that of the IR775-Cbl group was as high as ~46.40%. The high rate of necrosis in the IR775-Cbl group most probably resulted from the impairment of mitochondrial function, the existence of mtDNA was more sensitive to possible alkylation due to the lack of a mitochondrial nucleic acid excision repair mechanism,[38,62,63] and even alkylation of mitochondrial proteins could potentially enhance its cytotoxicity and lead to rapid cell death.[64,65] Overall, the inhibition efficacy of alkylating drugs could be improved *via* functionalization with mitochondrial targeting moieties.[38]

Furthermore, the MCF-7 cell line, one of the most extensively studied human breast cancer cell lines, was selected to evaluate the cellular inhibition potency of the drug conjugate. Typical Annexin V-FITC/PI double staining of MCF-7 cells after diverse treatments was performed and quantitatively evaluated by flow cytometry analysis (Fig. S11†). Compared with other groups, IR775-Cbl led to a higher rate of cell necrosis at the same dosage, which mostly resulted from the highly specific accumulation of IR775-Cbl in the mitochondria. Apart from

probable *in situ* alkylation by an *in situ* high dosage of IR775-Cbl in the mitochondria, the rigid hydrophobic segment in IR775-Cbl could in principle also destroy the mitochondrial membrane mainly composed of amphiphilic lipids and proteins.[64]

In addition, MTT assays were employed to evaluate the *in vitro* cytotoxicity of IR775-Cbl against EMT6 cells (Fig. 4C). As observed, the cytotoxicity of Cbl was almost negligible over the whole concentration range, while the tumor cell inhibition of IR775 and IR775/Cbl mixture were also compromised in the tested range. Notably, the cytotoxicity of IR775-Cbl was much higher than that of the other experimental groups, and the toxicity increased along with the increase in administrated dosage. The content range of Cbl was further improved for cytotoxicity analysis (Fig. S12†). Taken together, the IC_{50} values of IR775-Cbl and Cbl were determined to be ~1.87 μM and ~409.3 μM, respectively, indicating a remarkable ~218.8-fold enhancement in cytotoxicity for Cbl after rational modification with IR775.[38] An extra human tumor cell line was accordingly also examined. MTT assays against MCF-7 cells were performed to examine the tumor cell inhibition potency (Fig. S13†). The tumor cell inhibition efficacy of IR775-Cbl was most prominent among the four groups, and the curve trend agreed with the result towards EMT6 cells. For comparison, the cytotoxicity of non-targeting TPE-Cbl was evaluated, suggesting unapparent cellular toxicity (Fig. S14†). Thus, the cytotoxicity of IR775-Cbl was postulated to mainly benefit from its mitochondrial targeting potency.[66]

Meanwhile, the morphological change in EMT6 cells was recorded with their bright field imaging (Fig. 4D). For comparison, the untreated blank cells were employed as the sample at 0 h. The untreated cells exhibited an adherent stretching configuration without abnormal shape change, upon incubation with IR775-Cbl for 4 h; some cells became slightly shrunken, whereas with an extension in incubation time to 8 h, most of the cells became round, and the ability to adhere to the culture dish became very weak. At 24 h, hardly any cells were found in the culture dish after gentle PBS washing (Fig. S15†). The cell TEM images further visualize the changes in cell morphology. The cells of the control group for the blank group had an intact morphology and well-maintained cell membranes, while the cells of the IR775-Cbl group showed obvious damage with ruptured cell membranes and solidified nuclei (Fig. S16†). The morphological change further verified the inhibition effect of IR775-Cbl towards EMT6 cells.

In vivo NIR imaging and tumor inhibition

Besides acting as a mitochondria-targeting moiety in IR775-Cbl, IR775 is also an NIR-emissive fluorogen; thus, it can be used for real-time fluorescence imaging in tumor theranostics.[67] To afford IR775-Cbl with optimized pharmacokinetics, an aqueous dispersion of IR775-Cbl@PF127 was formulated from the co-assembly of IR775-Cbl and Pluronic F-127 (PF127).[68] The formulation content of IR775-Cbl in the resultant dispersion was determined from the standard curve of IR775-Cbl (Fig. S17†). TEM analysis revealed spherical nanostructures for self-assembled micelles with an average size of ~80 nm, and the hydrodynamic diameter was measured by DLS to be ~135 nm (Fig. S18A†). The zeta potential of the IR775-Cbl@PF127 dispersion was recorded to be nearly neutral at ~−1.23 mV due to the protection of hydrophilic corona. In addition, the size variation was insignificant after one week of storage at room temperature; thus, the micellar dispersion displayed favorable aqueous stability (Fig. S18B†). In addition, the serum stability was explored in FBS and 1640 cell culture medium containing 10% FBS at 37 °C, (Fig. S19†). The results showed that IR775-Cbl@PF127 maintained good stability in FBS and 1640 culture medium containing 10% FBS, with insignificant changes in hydrodynamic diameter, showing good colloidal stability.[69] In contrast, IR775-Cbl showed insignificant changes in particle size in FBS, but fluctuated more in 1640 containing 10% FBS. This suggests that the co-assembly of PF127 with IR775-Cbl improved its colloidal stability in serum, which is favorable for subsequent biomedical applications.[70] The *in vivo* biodistribution was evaluated against EMT6 tumor-bearing mice (Fig. 5A). Upon intravenous injection with an aqueous dispersion of IR775-Cbl@PF127 for 3 h, the fluorescence signal at the tumor site reached its maximum, which remained strong and observable over the whole duration of the experiment even up to 24 h post-injection (Fig. 5A). Thus, IR775-Cbl@PF127 could effectively accumulate and be retained at the tumor site for over 24 h. The biodistribution of IR775 *in vivo* was also analyzed by fluorescence imaging (Fig. S20†). As observed, IR775 did not significantly accumulate at the tumor site. At the same time, the fluorescence imaging of the main organs and tumors was observed 24 h after treatment. Besides the liver and kidneys, IR775 exhibited strong fluorescence in the heart and lungs, indicating potential organ toxicity, and PF127@IR775-Cbl could alleviate above shortcomings.

Encouraged by the superior tumor cell inhibition of IR775-Cbl, *in vivo* tumor inhibition was evaluated to examine the therapeutic efficacy of IR775-Cbl. Previously, the cellular uptake of IR775-Cbl@PF127 was evaluated at the cellular level. The cellular uptake efficiency was significantly improved compared to IR775-Cbl, suggesting the possibility of enhanced efficacy (Fig. S21†). EMT6 tumor-bearing mice were established by subcutaneous injection of EMT6 cells into the flanks of female BALB/c mice (Fig. 5B). The mice were divided into six groups and treated by tail vein injection. The mice were treated every three days, and the body weight and tumor volume of the mice were recorded simultaneously during all six treatments. Compared with the PBS group, the Cbl group, the IR775 group, and the IR775/Cbl mixture group showed only mild tumor inhibition, while the IR775-Cbl group further exhibited much better inhibition than that of the abovementioned three groups. Notably, the IR775-Cbl@PF127 group exhibited the most significant tumor inhibition, which presumably benefited from its favorable pharmacokinetics compared with the IR775-Cbl group (Fig. 5C–E).[71] Moreover, representative H&E images of collected tumors from each group showed that more dense cells with highly condensed nuclei

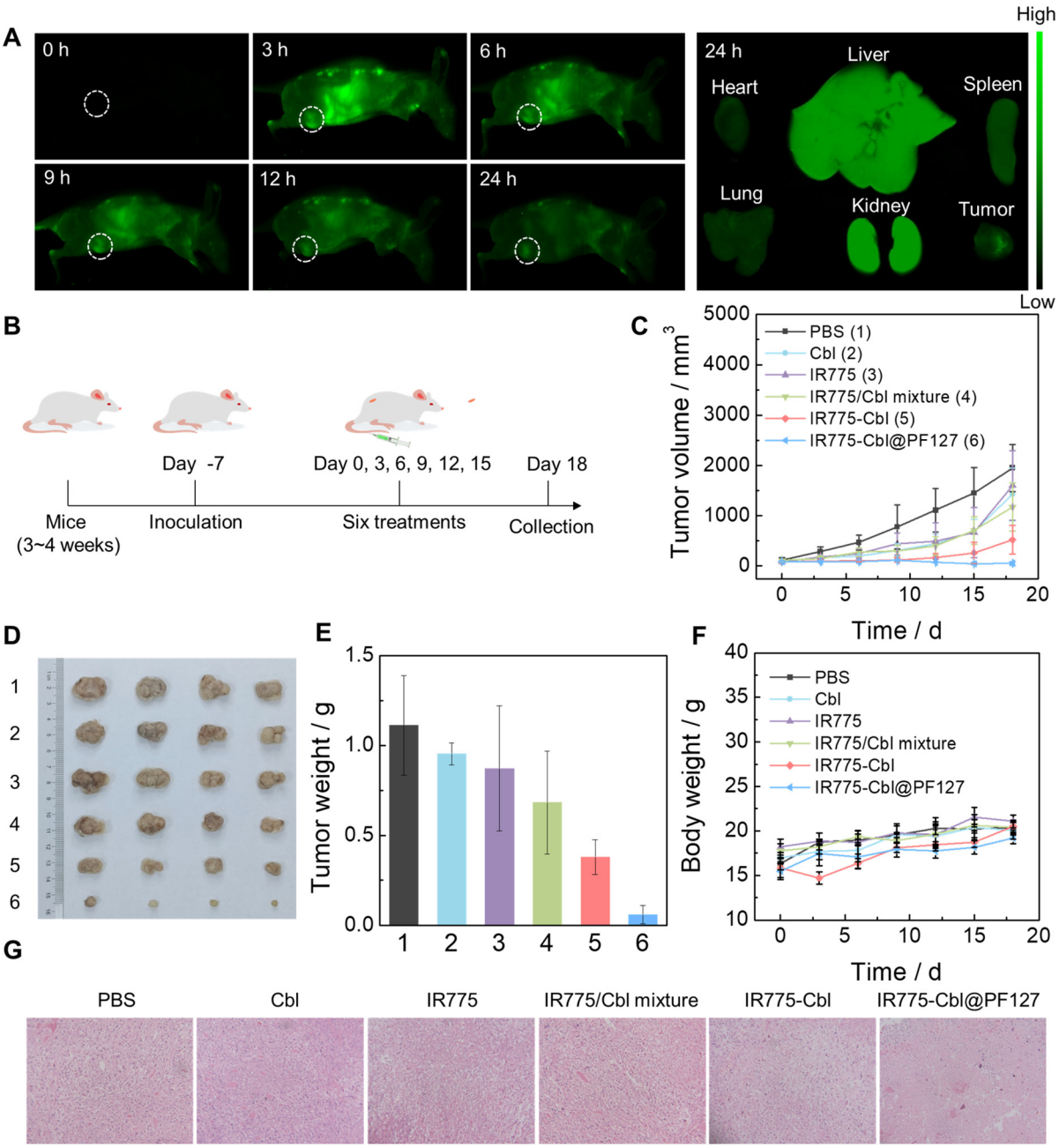

Fig. 5 *In vivo* tumor imaging and inhibition. (A) Fluorescence imaging of EMT6 tumor-bearing mice upon intravenous injection with IR775-Cbl@PF127 and typical fluorescent images of major organs and tumors collected at 24 h post-injection. (B) Schematics for *in vivo* tumor inhibition against EMT6 tumor-bearing mice. (C) Tumor growth curves during the treatment process. (D) Typical tumor photographs collected from various groups after diverse treatments. (E) Tumor weight of (D). (F) Body weight of EMT6 tumor-bearing mice in various groups in the treatment process. (Mean ± SD, n = 4). (G) Representative H&E images (20×) of tumor samples collected from different groups after diverse treatments.

appeared in the IR775-Cbl and IR775-Cbl@PF127-treated groups, which were generally considered to be dead tumor cells (Fig. 5G).

During the whole treatment process, no significant difference in body weight was observed among all the treatment groups, indicating no obvious systemic toxicity during the treatments (Fig. 5F). Finally, histological analysis of the major organs was performed for the mice in different groups, and no obvious signal of organ damage was observed in any of the groups; thus, potential side effects towards major organs were minimal (Fig. S22†). Meanwhile, hemolysis tests revealed that IR775-Cbl@PF127 displayed a minimal hemolytic ratio, <5% even at an equivalent IR775-Cbl dosage of 20 μM. For comparison, a native IR775-Cbl aqueous dispersion showed a slightly elevated hemolytic ratio, <12% at 20 μM, which was also acceptable in practical applications.[72] The presence of PF127 defi-

nitely reduced the positive charge exposure of IR775-Cbl and further enhanced the biocompatibility of the drug aggregates for *in vivo* applications (Fig. S23†).[73] These results suggested that current theranostic conjugate-formulated polymeric nanoparticles had superior safety and minimal side effects, which lays down a solid foundation for promising clinical translation.

Conclusions

In summary, Cbl is one of the oldest chemotherapeutic agents commonly used for the treatment of chronic lymphocytic leukemia, ovarian cancer, and low-grade malignant non-Hodgkin's lymphoma. This work asked whether there were new opportunities to potentiate its native chemotherapeutic efficacy *via* covalent modification with a mitochondria-targeting NIR fluorophore. Upon facile tethering with IR775, the resultant IR775-Cbl conjugate could readily self-assemble into spherical nanostructures with favorable aqueous stability. Cbl has rarely been used for the treatment of breast tumor due to its limited efficacy and serious side effects, while the resultant IR775-Cbl demonstrated superior inhibition towards a breast tumor model. IR775-Cbl was observed to selectively target the mitochondria of tumor cells, triggering serious mitochondrial dysfunction and rapid cell death, and achieving a significant "1 + 1 > 2" amplifying effect *in vitro* and *in vivo* compared with IR775 or CbI or an IR775/Cbl mixture. Furthermore, the presence of IR775 in IR775-Cbl guaranteed that the drug conjugate could be discernable for real-time monitoring *in vivo*. The current facile modification strategy with a mitochondria-targeting NIR dye is promising for endowing traditional drugs with subcellular targeting, imaging, and remarkable therapeutic efficacy. The simple nature of this method is helpful for promoting clinical translation. Furthermore, the application field of this work is not limited to tumor theranostics and is probably suitable for other diseases.

Author contributions

JL and JZ contributed equally to the experimental performing, data collection and analysis, and manuscript preparation. YTZ, WW, and MXZ contributed to *in vitro* and animal experiments. ZRZ, BL, XLH and WLH contributed to the study conception and design, data interpretation and manuscript revision. All the authors have read and approved the current version of the manuscript.

Ethical statement

All procedures of animal experiments were approved by the Animal Care and Use Committee of South China Normal University (SCNU-BIP-2024-025)

Conflicts of interest

The authors declare no competing interests.

Acknowledgements

This work was supported by the National Natural Science Foundation of China (81871994 and 82022037), Guangdong Basic and Applied Basic Research Foundation (2021B1515230009), and Guangdong Provincial Key Laboratory of Tumor Interventional Diagnosis and Treatment (2021B1212040004).

References

1 K. D. Miller, L. Nogueira, A. B. Mariotto, J. H. Rowland, K. R. Yabroff, C. M. Alfano, A. Jemal, J. L. Kramer and R. L. Siegel, *CA Cancer J. Clin.*, 2019, **69**, 363–385.
2 F. Zhou, P. Wang, Y. Peng, P. Zhang, Q. Huang, W. Sun, N. He, T. Fu, Z. Zhao, X. Fang and W. Tan, *Angew. Chem., Int. Ed.*, 2019, **58**, 11661–11665.
3 X. Hu, J. Hu, J. Tian, Z. Ge, G. Zhang, K. Luo and S. Liu, *J. Am. Chem. Soc.*, 2013, **135**, 17617–17629.
4 Y. Zhang, P. He, P. Zhang, X. Yi, C. Xiao and X. Chen, *Adv. Healthcare Mater.*, 2021, **10**, 2001974.
5 J. Shi, P. W. Kantoff, R. Wooster and O. C. Farokhzad, *Nat. Rev. Cancer*, 2017, **17**, 20–37.
6 C. Li, J. Wang, Y. Wang, H. Gao, G. Wei, Y. Huang, H. Yu, Y. Gan, Y. Wang, L. Mei, H. Chen, H. Hu, Z. Zhang and Y. Jin, *Acta Pharm. Sin. B*, 2019, **9**, 1145–1162.
7 Y. Wang, Z. Luo, D. Zhou, X. Wang, J. Chen, S. Gong and Z. Yu, *Biomater. Sci.*, 2021, **9**, 4110–4119.
8 W. Gu, F. Meng, R. Haag and Z. Zhong, *J. Controlled Release*, 2021, **329**, 676–695.
9 B. Guo, Z. Huang, Q. Shi, E. Middha, S. Xu, L. Li, M. Wu, J. Jiang, Q. Hu, Z. Fu and B. Liu, *Adv. Funct. Mater.*, 2020, **30**, 1907093.
10 Z. Deng and S. Liu, *Polymer*, 2020, **207**, 122914.
11 Y. Zhong, F. Meng, C. Deng and Z. Zhong, *Biomacromolecules*, 2014, **15**, 1955–1969.
12 D. Cao, H. He, W. Li, J. Yan, J. Wu, M. Yin, Y. Zhou, Z. Zhou and L. Yin, *Biomater. Sci.*, 2021, **9**, 4054–4065.
13 P. a. Ma, H. Xiao, C. Yu, J. Liu, Z. Cheng, H. Song, X. Zhang, C. Li, J. Wang, Z. Gu and J. Lin, *Nano Lett.*, 2017, **17**, 928–937.
14 J. Siepmann, A. Faham, S.-D. Clas, B. J. Boyd, V. Jannin, A. Bernkop-Schnürch, H. Zhao, S. Lecommandoux, J. C. Evans, C. Allen, O. M. Merkel, G. Costabile, M. R. Alexander, R. D. Wildman, C. J. Roberts and J.-C. Leroux, *Int. J. Pharm.*, 2019, **558**, 128–142.
15 B. Geers, O. De Wever, J. Demeester, M. Bracke, S. C. De Smedt and I. Lentacker, *Small*, 2013, **9**, 4027–4035.
16 Y. Zhong, F. Meng, W. Zhang, B. Li, J. C. M. van Hest and Z. Zhong, *J. Controlled Release*, 2020, **320**, 421–430.

17 J. Wang, W. Mao, L. L. Lock, J. Tang, M. Sui, W. Sun, H. Cui, D. Xu and Y. Shen, *ACS Nano*, 2015, **9**, 7195–7206.
18 F. Liu, L. Lin, Y. Zhang, S. Sheng, Y. Wang, C. Xu, H. Tian and X. Chen, *Biomaterials*, 2019, **223**, 119470.
19 G. Shim, M.-G. Kim, J. Y. Park and Y.-K. Oh, *Adv. Drug Delivery Rev.*, 2016, **105**, 205–227.
20 P. Zhang, A. G. Cheetham, Y.-a. Lin and H. Cui, *ACS Nano*, 2013, **7**, 5965–5977.
21 X. Zhen, J. Zhang, J. Huang, C. Xie, Q. Miao and K. Pu, *Angew. Chem., Int. Ed.*, 2018, **57**, 7804–7808.
22 J. Zhang, B. Zhao, S. Chen, Y. Wang, Y. Zhang, Y. Wang, D. Wei, L. Zhang, G. Rong, Y. Weng, J. Hao, B. Li, X.-Q. Hou, X. Kang, Y. Zhao, F. Wang, Y. Zhao, Y. Yu, Q.-P. Wu, X.-J. Liang and H. Xiao, *ACS Nano*, 2020, **14**, 14831–14845.
23 J. Qi, H. Ou, Q. Liu and D. Ding, *Aggregate*, 2021, **2**, 95–113.
24 D. Huo, X. Jiang and Y. Hu, *Adv. Mater.*, 2020, **32**, 1904337.
25 Y. Zhang, F. Fang, L. Li and J. Zhang, *ACS Biomater. Sci. Eng.*, 2020, **6**, 4816–4833.
26 D. Gao, Y. Shi, J. Ni, S. Chen, Y. Wang, B. Zhao, M. Song, X. Guo, X. Ren, X. Zhang, Z. Tian and Z. Yang, *Small*, 2021, 2106000.
27 H. Ye, Y. Xian, S. Li, C. Zhang and D. Wu, *Biomater. Sci.*, 2022, **10**, 4218–4227.
28 S. Wang, G. Yu, W. Yang, Z. Wang, O. Jacobson, R. Tian, H. Deng, L. Lin and X. Chen, *Adv. Sci.*, 2021, **8**, 2002927.
29 C. Yao, Y. Li, Z. Wang, C. Song, X. Hu and S. Liu, *ACS Nano*, 2020, **14**, 1919–1935.
30 P. Huang, D. Wang, Y. Su, W. Huang, Y. Zhou, D. Cui, X. Zhu and D. Yan, *J. Am. Chem. Soc.*, 2014, **136**, 11748–11756.
31 S. Chen, D. Li, X. Du, X. He, M. Huang, Y. Wang, X. Yang and J. Wang, *Nano Today*, 2020, **35**, 100924.
32 R. Zhang, R. Xing, T. Jiao, K. Ma, C. Chen, G. Ma and X. Yan, *ACS Appl. Mater. Interfaces*, 2016, **8**, 13262–13269.
33 D. Zheng, Y. Chen, S. Ai, R. Zhang, Z. Gao, C. Liang, L. Cao, Y. Chen, Z. Hong, Y. Shi, L. Wang, X. Li and Z. Yang, *Research*, 2019, **2019**, 4803624.
34 A. G. Cheetham, R. W. Chakroun, W. Ma and H. Cui, *Chem. Soc. Rev.*, 2017, **46**, 6638–6663.
35 J. Xiang, X. Liu, G. Yuan, R. Zhang, Q. Zhou, T. Xie and Y. Shen, *Adv. Drug Delivery Rev.*, 2021, **179**, 114027.
36 J. Zhang, B. Zhao, S. Chen, Y. Wang, Y. Zhang, Y. Wang, D. Wei, L. Zhang, G. Rong, Y. Weng, J. Hao, B. Li, X.-Q. Hou, X. Kang, Y. Zhao, F. Wang, Y. Zhao, Y. Yu, Q.-P. Wu, X.-J. Liang and H. Xiao, *ACS Nano*, 2020, **14**, 16159–16160.
37 Q. Guo, Y. Liu, G. Mu, L. Yang, W. Wang, J. Liu and J. Liu, *Biomater. Sci.*, 2020, **8**, 5638–5646.
38 M. Millard, J. D. Gallagher, B. Z. Olenyuk and N. Neamati, *J. Med. Chem.*, 2013, **56**, 9170–9179.
39 J. Zhuang, N. Li, Y. Zhang, B. Li, H. Wen, X. Zhang, T. Zhang, N. Zhao and B. Z. Tang, *CCS Chem.*, 2022, **4**, 1028–1043.
40 S. E. Weinberg and N. S. Chandel, *Nat. Chem. Biol.*, 2015, **11**, 9–15.
41 L. Jiang, S. Zhou, X. Zhang, C. Li, S. Ji, H. Mao and X. Jiang, *Nat. Commun.*, 2021, **12**, 2390.
42 X. Guo, N. Yang, W. Ji, H. Zhang, X. Dong, Z. Zhou, L. Li, H.-M. Shen, S. Q. Yao and W. Huang, *Adv. Mater.*, 2021, **33**, 2007778.
43 H. B. Ruttala, T. Ramasamy, R. R. T. Ruttala, T. H. Tran, J.-H. Jeong, H.-G. Choi, S. K. Ku, C. S. Yong and J. O. Kim, *J. Mater. Sci. Technol.*, 2021, **86**, 139–150.
44 X. Liu, H.-R. Jia, Y.-X. Zhu, G. Gao, Y.-W. Jiang, X. Cheng, K.-F. Xu, X.-W. Yu and F.-G. Wu, *Sci. China Mater.*, 2020, **63**, 851–863.
45 R. G. Thomas and Y. Y. Jeong, *Chonnam Med. J.*, 2017, **53**, 83–94.
46 E. Zhang, S. Luo, X. Tan and C. Shi, *Biomaterials*, 2014, **35**, 771–778.
47 M. M. Leitão, D. de Melo-Diogo, C. G. Alves, R. Lima-Sousa and I. J. Correia, *Adv. Healthcare Mater.*, 2020, **9**, 1901665.
48 Z. Zhao, X. Zhang, H. Zhang, X. Shan, M. Bai, Z. Wang, F. Yang, H. Zhang, Q. Kan, B. Sun, J. Sun, Z. He and C. Luo, *Adv. Sci.*, 2022, **9**, 2104264.
49 Y.-F. Xiao, F.-F. An, J.-X. Chen, J. Yu, W.-W. Tao, Z. Yu, R. Ting, C.-S. Lee and X.-H. Zhang, *Small*, 2019, **15**, 1903121.
50 U. S. Dinish, Z. Song, C. J. H. Ho, G. Balasundaram, A. B. E. Attia, X. Lu, B. Z. Tang, B. Liu and M. Olivo, *Adv. Funct. Mater.*, 2015, **25**, 2316–2325.
51 C. Wu, R. Zhang, W. Du, L. Cheng and G. Liang, *Nano Lett.*, 2018, **18**, 7749–7754.
52 S. Zhai, X. Hu, Y. Hu, B. Wu and D. Xing, *Biomaterials*, 2017, **121**, 41–54.
53 X. Li, M. Yang, J. Cao, H. Gu, W. Liu, T. Xia, W. Sun, J. Fan and X. Peng, *ACS Mater. Lett.*, 2022, **4**, 724–732.
54 F. Wu, Y. Lu, X. Mu, Z. Chen, S. Liu, X. Zhou, S. Liu and Z. Li, *ACS Appl. Mater. Interfaces*, 2020, **12**, 32388–32396.
55 M. Kang, Z. Zhang, N. Song, M. Li, P. Sun, X. Chen, D. Wang and B. Z. Tang, *Aggregate*, 2020, **1**, 80–106.
56 S. Luo, X. Tan, S. Fang, Y. Wang, T. Liu, X. Wang, Y. Yuan, H. Sun, Q. Qi and C. Shi, *Adv. Funct. Mater.*, 2016, **26**, 2826–2835.
57 W. Zhang, X. Hu, Q. Shen and D. Xing, *Nat. Commun.*, 2019, **10**, 1704.
58 N. A. Bonekamp, B. Peter, H. S. Hillen, A. Felser, T. Bergbrede, A. Choidas, M. Horn, A. Unger, R. Di Lucrezia, I. Atanassov, X. Li, U. Koch, S. Menninger, J. Boros, P. Habenberger, P. Giavalisco, P. Cramer, M. S. Denzel, P. Nussbaumer, B. Klebl, M. Falkenberg, C. M. Gustafsson and N.-G. Larsson, *Nature*, 2020, **588**, 712–716.
59 Z. Wang, M. Zhan, W. Li, C. Chu, D. Xing, S. Lu and X. Hu, *Angew. Chem., Int. Ed.*, 2021, **60**, 4720–4731.
60 Q. W. Chen, X. H. Liu, J. X. Fan, S. Y. Peng, J. W. Wang, X. N. Wang, C. Zhang, C. J. Liu and X. Z. Zhang, *Adv. Funct. Mater.*, 2020, **30**, 1909806.
61 W. Zhang, X.-F. Du, B. Liu, C. Li, J. Long, M.-X. Zhao, Z. Yao, X.-J. Liang and Y. Lai, *ACS Nano*, 2022, **16**, 1421–1435.

62 H. Zhang, J. Liu, Y.-Q. Sun, M. Liu and W. Guo, *J. Am. Chem. Soc.*, 2020, **142**, 17069–17078.
63 Y. B. Peng, Z. L. Zhao, T. Liu, G. J. Xie, C. Jin, T. G. Deng, Y. Sun, X. Li, X. X. Hu, X. B. Zhang, M. Ye and W. H. Tan, *Chem. – Eur. J.*, 2017, **12**, 250–256.
64 S. R. Jean, M. P. Pereira and S. O. Kelley, *Mol. Pharmaceutics*, 2014, **11**, 2675–2682.
65 S. B. Fonseca, M. P. Pereira, R. Mourtada, M. Gronda, K. L. Horton, R. Hurren, M. D. Minden, A. D. Schimmer and S. O. Kelley, *Chem. Biol.*, 2011, **18**, 445–453.
66 H. Wang, R. Wang, K. Cai, H. He, Y. Liu, J. Yen, Z. Wang, M. Xu, Y. Sun, X. Zhou, Q. Yin, L. Tang, I. T. Dobrucki, L. W. Dobrucki, E. J. Chaney, S. A. Boppart, T. M. Fan, S. Lezmi, X. Chen, L. Yin and J. Cheng, *Nat. Chem. Biol.*, 2017, **13**, 415–424.
67 H. Liang, X. Chen, R. Jin, B. Ke, M. Barz, H. Ai and Y. Nie, *Small*, 2020, **16**, 1906538.
68 G.-M. Zhang, D. Jiao, S.-C. Nie, Z.-Y. Xu, X. Zhang, Y. Dai, M.-N. Jiao, H. Ou, Y.-B. Yan and D. Ding, *Biomater. Sci.*, 2022, **10**, 1929–1935.
69 Z. Sun, M. Ren, B. Shan, Q. Yang, Z. Zhao, X. Liu and L. Yin, *Biomater. Sci.*, 2023, **11**, 5653–5662.
70 H. Li, Y. Fu, T. Zhang, Y. Li, X. Hong, J. Jiang, T. Gong, Z. Zhang and X. Sun, *Adv. Funct. Mater.*, 2015, **25**, 7457–7469.
71 X. Cai, Z. Xie, B. Ding, S. Shao, S. Liang, M. Pang and J. Lin, *Adv. Sci.*, 2019, **6**, 1900848.
72 Y. Zhang, X. He, Y. Zhang, Y. Zhao, S. Lu, Y. Peng, L. Lu, X. Hu and M. Zhan, *Chem. Eng. J.*, 2021, **424**, 130171.
73 J. Xia, Q. Pei, M. Zheng and Z. Xie, *J. Mater. Chem. B*, 2021, **9**, 2308–2313.